Microwave imaging of mesoscopic percolating network in a manganite thin film

Keji Lai,[1] Masao Nakamura,[2] Worasom Kundhikanjana,[1] Masashi
Kawasaki,[2,3] Yoshinori Tokura,[2,4] Michael A. Kelly,[1] and Zhi-Xun Shen[1]

[1]*Department of Applied Physics and Geballe Laboratory for Advanced Materials, Stanford University, Stanford, CA 94305*
[2]*Cross-Correlated Materials Group (CMRG), ASI, RIKEN, Wako, 351-0198, Japan*
[3]*WPI-Advanced Institute for Materials Research (AIMR), Tohoku University, Sendai, 980-8577, Japan*
[4]*Department of Applied Physics, University of Tokyo, Tokyo 113-8586, Japan*
(Dated: July 19, 2010)

Many unusual behaviors in complex oxides are deeply associated with the spontaneous emergence of microscopic phase separation. Depending on the underlying mechanism, the competing phases can form ordered or random patterns at vastly different length scales. Using a microwave impedance microscope, we observed an orientation-ordered percolating network in strained $Nd_{0.5}Sr_{0.5}MnO_3$ thin films with a large period of 100 nm. The filamentary metallic domains align preferentially along certain crystal axes of the substrate, suggesting the anisotropic elastic strain as the key interaction in this system. The local impedance maps provide microscopic electrical information of the hysteretic behavior in strained thin film manganites, suggesting close connection between the glassy order and the colossal magnetoresistance effects at low temperatures.

PACS numbers:

Doped cuprate superconductors and colossal magnetoresistive (CMR) manganites, the two most studied complex oxides, exhibit rich phase diagrams as a result of the simultaneously active charge, spin, orbital, and lattice degrees of freedom [1, 2]. Recent work on these strongly correlated materials has shown that multiple states can coexist near certain phase boundaries, a scenario known as microscopic phase separation [1]. The configurations of these spatially inhomogeneous phases reflect the underlying interactions. When the long-range Coulomb interaction prevails, the competing phases usually form nanometer-scale orders, because of the electrostatic energy penalty for macroscopic phase separation [3–6]. For self-organized patterns at larger length scales, weaker long-range interactions, such as the elastic strain arising from either the cooperative lattice distortions or lattice mismatch between substrates and epitaxial thin films, become the dominant factors [7–9]. Finally, the unavoidable quenched disorders in real materials always introduce short-range potential fluctuations, which usually smear out the orders or even result in micrometer-sized clusters with random shapes [10].

Many physical properties affected by the phase separation, such as the local density of states [4–6, 11, 12], the local magnetization [13–15], and the atomic displacement [16], can be spatially mapped out by established microscopy tools. For CMR manganites with drastic resistance changes at different temperatures (T) and magnetic fields (H), the local resistivity (ρ) has a large span that makes spatially resolved DC measurements challenging. Imaging with high-frequency AC-coupled local probes is thus desirable. We carried out a microwave impedance microscopy (MIM) study [17, 18] on manganite thin films. Unlike other GHz microscopes [19], the cantilever probe is well shielded to reduce the stray fields [18]. In the mi-

crowave electronics, the high-Q resonator [20] susceptible to environmental conditions is eliminated so that the system can be implemented under variable temperatures (2-300K) and high magnetic fields (9T). Our cryogenic MIM is therefore a versatile tool to investigate various electronic phase transitions. Only the imaginary part of the tip-sample impedance is presented here as the local resistivity information is fully captured by the capacitive channel (MIM-C).

We study $Nd_{0.5}Sr_{0.5}MnO_3$ (NSMO) thin films grown on (110) $SrTiO_3$ (STO) substrates by pulsed-laser deposition. In single crystal NSMO, both resistivity and magnetization measurements show a paramagnetic (PM) to ferromagnetic (FM) transition at the Curie temperature $T_C \sim 250K$ and a charge/orbital-order (COO) transition at $T_{COO} \sim 160K$ [21]. When a magnetic field is turned on at temperatures below T_{COO}, a dramatic first-order phase transition from the antiferromagnetic COO insulating (COO-I) state to the FM metallic (FM-M) state is observed. We emphasize that two types of CMR, the T-driven PM-FM CMR and the low-T H-driven CMR, are widely discussed in the literature [22] and we only focus on the latter in this work. Recent effort in this model system has been devoted to epitaxial films [23, 24]. To date, bulk-like behaviors are only seen for films grown on (110) STO substrates, presumably due to the strong dependence on the lattice strain. Even on the same substrate, sample degradation resulting from partial loss of crystalinity and epitaxial coherency is sometimes detected. We present data from two samples, sample a in which clear signatures of T_C and T_{COO} are present (Fig. 1A), and, for comparison, a degraded sample b, which lacks metallic temperature regions. The samples were characterized by atomic force microscope (AFM, Fig. 1B) and cross-sectional transmission electron microscope (TEM, Fig.
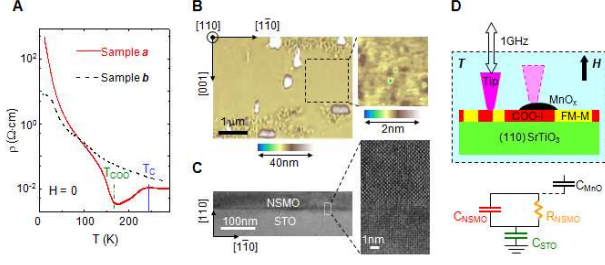
FIG. 1: (A) Zero-field (T) curves of two samples a (30nm NSMO/STO) and b (60nm NSMO/STO). The metallic temperature region between the bulk T_C (blue) and T_{COO} (green) is present in sample a but missing in sample b. At low-T, ρ_a(T) diverges and ρ_b(T) saturates. (B) The AFM surface topography contains MnO_x precipitates ($\sim$20nm in height) and corrugations. Crystal axes of the STO substrate are indicated. The close-up shows an atomically-flat region 1$\sim$2μm in size. Note the different false-color scales between the main figure (40nm) and the close-up (2nm). (C) Cross-sectional TEM image of the NSMO-STO interface of sample a. The good crystalinity and coherent epitaxy are confirmed by a close-up high-resolution TEM picture. (D) Schematics of the system setup (top) and the corresponding lumped-element circuit (bottom). When the tip scans over the FM-M domains (yellow), the small R_{NSMO} shunts the capacitor C_{NSMO}, giving a larger signal than that of the COO-I background (red). The insulating particles (black), on the other hand, introduce a series capacitor (C_{MnO}), resulting in lower MIM-C signals.

1C). The surface contains micrometer-sized precipitates, most likely MnO_x [25], and some corrugations next to these particles. In between the defective regions, there exist atomically flat areas where pure electrical signals can be obtained. The contrast in MIM-C images is qualitatively understood by the lumped-element circuit in Fig. 1D.

Simultaneously taken transport data and low-T microwave images are shown in Figs. 2A-D for sample a and Fig. 2E for sample b. Both the DC voltage and microwave excitation were kept low to avoid any extrinsic perturbation. The insulating MnO_x particles behaved as field-independent markers. At low fields where ρ barely decreases, some rod-like FM-M domains (indicated by blue arrows) tilted with respect to the [001] direction were observed on the COO-I background in both samples. The presence of such low-field conducting domains implies that phase separation already occurs before the H-field is turned on. We note that sample b showed larger low-field FM-M areal fraction than sample a. As H was increased to 6$\sim$7T, metallic areas grew from the low-field nucleation sites; their positions and shapes indicate a certain memory effect [26]. In a subsequent experiment, sample a was warmed up to 250K and cooled back to 15K at H = 0. A field of 6.5T was turned on after this thermal cycle. Most FM-M domains, as shown in the left inset of Fig. 2C, reappeared in the same locations

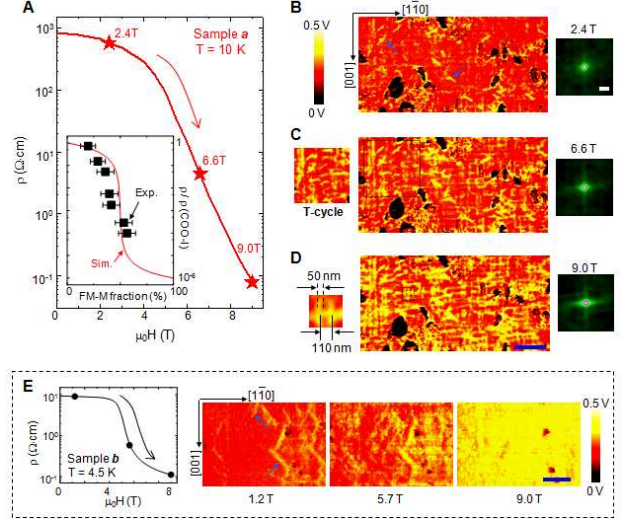FIG. 2: (A) ρ_a(H) during the field sweep at T = 10K. The three fields at which MIM images in (B-D) were taken are labeled by the red stars. Inset, comparison between the 2D square-lattice simulation ($\rho_{COO-I} \sim 10^3\Omega$.cm and $\rho_{FM-M} \sim 10^{-3}\Omega$.cm) and the experimental data. The large error bars and deviations near the percolation transition may result from the surface defects, the finite resolution, and the fact that percolation in NSMO is 3D in nature. (B-D) Microwave images (scale bar 1μm) taken at 10K and under μ_0H = 2.4T, 6.6T, and 9.0T, respectively. MnO_x particles appear black in the images. At low fields, some isolated rod-like FM-M domains (yellow) are indicated by blue arrows. Left inset of (C), measurement taken at 15K and 6.5T after a thermal cycle. Left inset of (D), close-up of a small region in (D) (black square) shows the typical width and spacing of the filaments. The center portions of auto-correlation image (scale bar 0.2μm) are shown on the right of (B-D), with a notable center-cross seen at 9.0T. (E) Transport and three MIM images (scale bar 1μm) of sample b taken at 4.5K. The low-field FM-M rods are indicated by arrows.

compared to the corresponding area in the main Fig. 2C (dotted box), indicative of pinning by an intrinsic long-range energy landscape and short-range disorder potentials. A striking distinction between the two samples at intermediate fields is that the H-induced FM-M filaments of sample a (Fig. 2C) show clear directional ordering and preferentially align along [001] and [1-10] axes of the substrate, whereas no such feature is seen in sample b within our spatial resolution. At 8$\sim$9T, the prominent FM-M filaments in sample a form an interconnected percolating network. While the smallest measured feature width (30-50nm) may be set by our spatial resolution, the typical spacing $\sim$100nm is clearly resolved here. As ρ_a(H) does not show any sign of saturation at 9T, the FM-M domains should further expand at higher fields. ρ_b(H), on the other hand, levels off at 9T, consistent with the nearly full coverage of FM-M regions.

The salient liquid-crystal-like metallic network accom-

panying the low-T CMR effect in sample a is not seen by structural characterization and must be electronic in origin. We can obtain some insight by comparing this result with experiments on other manganites. Nanometer-sized domains with no preferred directions were observed in $La_{1-x}Ca_xMnO_3$ [11, 27] due to Coulomb interaction. Large sub-micrometer clusters with no particular shapes were imaged in $(La,Pr)_{1-x}Ca_xMnO_3$ [16] owing to the strong disorders. In the NSMO films, the elastic strain must play a vital role since neither Coulomb interaction nor quenched disorders can generate such mesoscopic ordered network [1–3]. It is likely that the accommodation strain [7, 14] between the pseudo-cubic FM-M and distorted orthorhombic COO-I phases is responsible for the low-field FM-M rods, which appear in both sample a and b. The more important epitaxial strain imposed by the (110) STO substrate [22, 23], which is crucial for producing the bulk-like behaviors, must account for the observed glassy orders in sample a. The lack of a universal form of phase separation in both the PM-FM [11, 27] and the low-T CMR effects [16] points to the robustness of the phenomenon - the effect occurs because of energetically competing states, while the exact CMR magnitude depends on detailed microscopic configurations.

Taking the areal fraction of FM-M states as the probability of connected bonds, we can compare the experimental data to the square-lattice random resistor network simulation [28, 29]. Despite some deviations near the threshold, the agreement between experiment and modeling in the inset of Fig. 2A shows that the low-T CMR is indeed percolative in nature. Second, the auto-correlation analysis is performed for Figs. 2B-D. The nearly circular auto-correlation peak at 2.4T evolves into a clear center-cross at 9T with a characteristic length $\sim 0.5 \mu m$. In analogy to the stripes or checkerboard patterns seen in cuprates [4–6], the 100nm period may be set by the long-range strain field, whereas the typical length of the filaments is determined by the strength of disorders. Interestingly, discernible anisotropy is seen in that the nematic domains along the [1-10] direction are statistically more favorable than the [001] direction, in fair agreement with the transport anisotropy observed in control samples. In the strained NSMO/(110)STO films, the in-plane lattice constant is locked to that of the substrate along the [001] direction while relaxed along the [1-10] direction [22, 23]. At the same time, the charge-ordered planes are parallel to the (100) or (010) planes. As the low-T CMR effect is accompanied by lattice deformation [21], the metallic domains may tend to expand along the more strain-free axis, resulting in the in-plane anisotropy. The nematic phase at this length scale provides a contrasting framework to understand the stripe phenomenon that also breaks in-plane C_2-symmetry at much shorter length scales [30].

The physical picture depicted above is further corroborated by results at elevated temperatures, as shown in
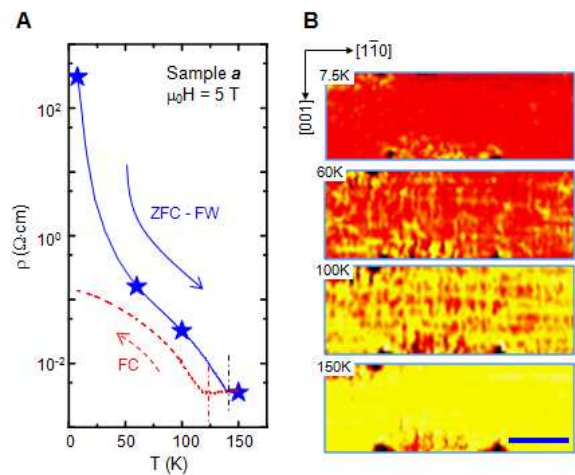

FIG. 3: (A) $\rho_a(T)$ at $\mu_0 H = 5T$ with the temperatures at (B) labeled. Before this experiment, sample a was cooled to 7.5K at H=0 followed by field sweep to 5T. The subsequent field-cool data (red dashed line) are also included. The up-turn temperatures (T_{COO}) are marked as dash-dot lines. (B) MIM images (scale bar $1\mu m$) taken by a second probe at 7.5K, 60K, 100K, and 150K from top to bottom, showing more FM-M domains at different temperatures. Due to the change of impedance match at different T, the full false-color scale is adjusted as 0.6V (7.5K), 0.7V (60K), 1.1V (100K), and 1.2V (150K), respectively.

Fig. 3. Before imaging, sample a was prepared by zero-field-cool (ZFC) to 7.5K and a field sweep to 5T. The field-warm (FW) resistivity data are shown in Fig. 3A. From 7.5K to 60K, considerable expansion of FM-M domains is seen, in conjunction with the resistivity drop by three orders of magnitude due to both thermal activation and percolation. At 100K, notable mesh-like FM-M network appears in the impedance map. For temperatures above $T_{COO} \sim 140K$ at 5T, the COO-I phases completely melt into metals, leaving only the insulating particles in the otherwise uniform sample.

In Fig. 3A, $\rho_a(T)$ during the cooling at 5T is also included, showing the marked hysteretic behavior widely observed in manganites. Using such field-cool (FC) process, one can access states with much lower than the ZFC process. Figs. 4A and 4B show the FC curves at four different fields and the corresponding microwave images taken at 12K, which is below T_{COO} for all fields. As H increases, the continuous COO-I phases at FC-2T break into isolated micrometer-sized domains (FC-7T), which continue to be percolated through by FM-M filaments (FC-8T) and shrink down to small droplets at FC-9T. Taking the transport signatures T_C and T_{COO}, we construct the phase diagram of this NSMO/STO sample in Fig. 4C, where phase coexistence is denoted below T_{COO}. The difference between the ZFC-FW and FC processes is shown by two lines separating the FM-M
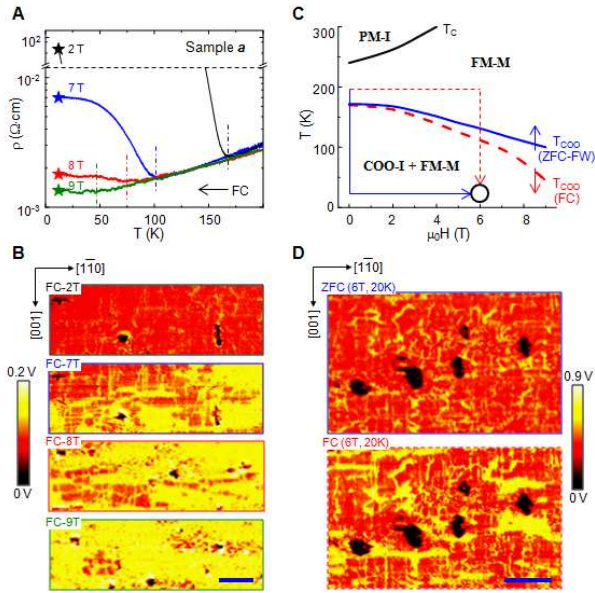
FIG. 4: (A) Field-cool resistivity and (B) MIM images (scale bar 1μm) at 2T, 7T, 8T, and 9T, respectively. T_{COO} is denoted by vertical dash-dot lines. (C) Phase diagram of sample a, showing the paramagnetic-insulator (PM-I), ferromagnetic-metal (FM-M) and phase coexistence (COO-I + FM-M) regions demarcated by transport signatures T_C or T_{COO} from ZFC-FW (field-warm, solid blue line) and FC (dashed red line) processes. Two paths from 200K, 0T to 20K, 6T are sketched in the plot. (D) MIM images (scale bar 1μm) taken at the same T = 20K and μ_0H = 6T. The FC image (bottom) contains much bigger conducting domains than the ZFC one (top).

and mixed phase regions. This phase diagram is reminiscent of the one for single crystal NSMO [21] except that the reentrant behavior reported there is beyond our field range. Using MIM, the microscopic origin of the hysteresis can be directly studied. In Fig. 4C, two paths arriving at the same external conditions are shown - the ZFC process from 200K to 20K followed by a field sweep to 6T, or field sweep to 6T at 200K before FC to 20K. The two MIM images in Fig. 4D display remarkably different percolating network. For the high-ρ (1.4Ω.cm) ZFC state, glassy FM-M filaments are again observed in the COO-I background. For the low-ρ (0.02Ω.cm) FC state, on the other hand, the FM-M phases occupy a much larger portion and even form micrometer-sized puddles elongated in the [1-10] direction. While hysteresis during the low-T CMR effect is known in single crystal NSMO from bulk

measurements, tools like MIM enable real space electrical imaging and demonstrate the strong dependence of phase separation on local disorders and strain fields near the multi-phase boundary.

[1] E. Dagotto, Science **309**, 257 (2005).
[2] Y. Tokura, Rep. Prog. Phys. **69**, 797 (2006).
[3] S. Yunoki et al., Phys. Rev. Lett. **80**, 845 (1998).
[4] M. Vershinin et al., Science **303**, 1995 (2004).
[5] T. Hanaguri et al., Nature **430**, 1001 (2004).
[6] C. Howald, H. Eisaki, N. Kaneko, M. Greven, and A. Kapitulnik, Phys. Rev. B **67**, 014533 (2003).
[7] N. D. Mathur and P. B. Littlewood, Solid State Commun. **119**, 271 (2001).
[8] K. H. Ahn, T. Lookman, and A. R. Bishop, Nature **428**, 401 (2004).
[9] J. Burgy, A. Moreo, and E. Dagotto, Phys. Rev. Lett. **92**, 097202 (2004).
[10] A. Moreo, M. Mayr, A. Feiguin, S. Yunoki, and E. Dagotto, Phys. Rev. Lett. **84**, 5568 (2000).
[11] M. Fath et al., Science **285**, 1540 (1999).
[12] Ch. Renner, G. Aeppli, B.-G. Kim, Yeong-Ah Soh, and S.-W. Cheong, Nature **416**, 518 (2002).
[13] L. Zhang, C. Israel, A. Biswas, R. L. Greene, and A. de Lozanne, Science **298**, 805 (2002).
[14] W. Wu et al., Nat. Mat. **5**, 881 (2006).
[15] J. C. Loudon, N. D. Mathur and P. A. Midgley, Nature **420**, 797 (2002).
[16] M. Uehara, S. Mori, C. H. Chen, and S.-W. Cheong, Nature **399**, 560 (1999).
[17] K. Lai, W. Kundhikanjana, M. Kelly, and Z. X. Shen, Rev. Sci. Instrum. **79**, 063703 (2008).
[18] K. Lai, W. Kundhikanjana, M. Kelly, and Z. X. Shen, Appl.Phy.Lett. **93**, 123105 (2008).
[19] B. T. Rosner and D. W. van der Weide, Rev. Sci. Instrum. **73**, 2505 (2002).
[20] Z. Wang et al., J. Appl. Phys. **92**, 808 (2002).
[21] H. Kuwahara, Y. Tomioka, A. Asamitsu, Y. Moritomo, and Y. Tokura, Science **270**, 961 (1995).
[22] H. Aliaga et al., Phys. Rev. B **68**, 104405 (2003).
[23] M. Nakamura, Y. Ogimoto, H. Tamaru, M. Izumi, and K. Miyano, Appl. Phys. Lett. **86**, 182504 (2005).
[24] Y. Wakabayashi et al., Phys. Rev. Lett. **96**, 017202 (2006).
[25] T. Higuchi et al., Appl. Phys. Lett. **95**, 043112 (2009).
[26] D. D. Sarma et al., Phys. Rev. Lett. **93**, 097202 (2004).
[27] J. Tao et al., Phys. Rev. Lett. **103**, 097202 (2009).
[28] S. Kirkpatrick, Rev. Mod. Phys. **45**, 574 (1973).
[29] M. Mayr et al., Phys. Rev. Lett. **86**, 135 (2001).
[30] J. A. Robertson, S. A. Kivelson, E. Fradkin, A. C. Fang, and A. Kapitulnik, Phys. Rev. B **74**, 134507 (2006).